PHYSICAL REVIEW A **89**, 013401 (2014)

Determination of Ar_2^+ and N_4^+ recombination coefficients by subpicosecond multiphoton ionization at 248 nm and microwave interferometry

K. E. Keister,[*] C. J. Wagner,[†] J. L. Putney,[‡] J. D. Hewitt,[§] and J. G. Eden
Laboratory for Optical Physics and Engineering, Department of Electrical and Computer Engineering,
University of Illinois, Urbana, Illinois 61801, USA

(Received 24 July 2013; published 3 January 2014)

Rate coefficients (α_D) for the dissociative recombination of Ar_2^+ and N_4^+ in low-temperature plasmas have been determined by multiphoton ionization of the parent gas (Ar or N_2) at 248 nm, in combination with microwave interferometry at 9.2 GHz. A subpicosecond, Ti:Al_2O_3-KrF hybrid laser system generating 40 mJ pulses at 248 nm serves as a photoionization source within one arm of an interferometer having a bandwidth of ~800 MHz, thereby providing an ultrafast (δ-function) plasma channel generator and a noninvasive, microwave probe of the plasma that together decouple the ionization mechanism (and source) from the electron detection process. Comparisons of measurements of the temporally resolved electron density with numerical simulations find α_D to be $(1.2-6.0) \times 10^{-6}$ $cm^3\,s^{-1}$ for Ar_2^+ and $(2 \pm 1) \times 10^{-6}$ $cm^3\,s^{-1}$ for N_4^+ for background pressures in the 150–600 Torr Ar and 10–400 Torr N_2 intervals, respectively. Both sets of constants are consistent with values reported previously in other ranges of gas pressure. The data and simulations indicate the cross section for four-photon ionization of Ar at 248 nm to be $(5 \pm 3) \times 10^{-118}$ $cm^8\,s^3$, or approximately 1.4 orders of magnitude lower than the single value in the literature [Uiterwaal *et al.*, Phys. Rev. A **57**, 392 (1998)]. Sub-50-ns transients observed in the electron density temporal profile for N_2 pressures above ~100 Torr suggest that the rate constant for $N_2(B)$-$N_2(B)$ associative ionization is almost an order of magnitude larger than the currently accepted value.

DOI: 10.1103/PhysRevA.89.013401 PACS number(s): 33.80.Rv, 34.80.Lx, 52.30.−q

I. INTRODUCTION

Electron-ion recombination in weakly ionized plasmas appears to have first been investigated experimentally by Kenty in 1928 [1]. However, it was not until the work of Biondi [2] in the early 1960s that dissociative recombination, represented by the reaction

$$(AB)^+ + e^- \xrightarrow{\alpha_D} A^* + B, \tag{1}$$

where the asterisk denotes an electronically excited state of a neutral atom (or molecule) and the rate coefficient α_D is expressed in units of $cm^3\,s^{-1}$, was understood to be the dominant electron loss mechanism for specific molecular ions such as those associated with the heavier rare gas dimers (Ne_2^+, Ar_2^+, Kr_2^+, and Xe_2^+). Earlier experiments [3–5] had measured electron density decay rates in low-temperature plasmas that were inconsistent with theoretical models assuming radiative recombination of an atomic ion ($A^+ + e^- \rightarrow A^* + \hbar\omega$) to be the sole electron loss process. The introduction of dissociative recombination resolved the discrepancy [2,6–8] and provided an electron density decay mechanism that is critical to describing the behavior of lasers [9], lamps [10], and other plasma devices and processes dependent upon the rare gases or nitrogen, for example. Previous measurements of the dissociative recombination coefficient for Ar_2^+ and N_4^+, in particular, have fallen into two pressure ranges: <30 Torr and >300 Torr. This order-of-magnitude gap between the pressure intervals investigated in the past is the result of purely experimental barriers associated with developing a suitable ionization source. Producing uniform glow discharges in the rare gases and nitrogen in a macroscopic volume (>1 cm^3) is problematic for pressures beyond 10–30 Torr because of localized heating of the gas and the subsequent emergence of streamers. An alternative approach to producing the necessary ionization rate is electron beam excitation [11–14] but significant absorption of the beam energy requires minimum background gas pressures of several hundred Torr. Furthermore, the repetition frequency of the source and the path length over which ionization can be sustained are restricted. Dissociative recombination of lighter molecular ions such as H_3^+ and HD^+ has also been investigated by merged-beam techniques [15,16] but past experiments appear to have not addressed the rare gas dimer ions, for example.

Measurements of the rate coefficients (α_D) governing the dissociative recombination of Ar_2^+ and N_4^+ are reported here. Multiphoton ionization of the parent molecule (Ar or N_2) in the deep ultraviolet is combined with microwave interferometry to provide measurements of the temporal history of the absolute electron density with a detection system having a bandwidth of 800 MHz. By generating a subpicosecond laser-produced plasma channel in one arm of an interferometer, electron loss rates can be determined directly from the temporal history of the electron density since deconvolution of the electron decay transient(s) from the plasma production (source) function is not necessary. That is, the laser provides an electron generation mechanism that is essentially a δ function in time, allowing for electron decay rates to be measured unambiguously. Values of α_D have been determined for Ar_2^+ and N_4^+ in the 150–600 Torr Ar and 10–400 Torr N_2 ranges, thus spanning the gap resulting from previous measurements in the literature.

---

[*] Present address: Earlham College, Richmond, Indiana 47374, USA.

[†] Present address: Philips Lighting, Ontario, California 91761, USA.

[‡] Present address: Diagnostic Photonics, Inc., Champaign, Illinois 61820, USA.

[§] Present address: Abilene Christian University, Abilene, Texas 79699, USA.

These coefficients, determined through detailed comparisons of the time-resolved electron density with numerical simulations, are consistent with existing values measured in other regions of background gas pressure. The Ar data conform well to a conventional kinetics model and the measured values of α_D are in agreement with previously reported coefficients obtained at higher ($150-1.2 \times 10^4$ Torr) and lower (1.9–50 Torr) Ar pressures. In contrast, simulations of electron density decay in laser-produced N_2 plasma channels do not predict an experimentally observed, sub-50-ns transient in the electron density that is attributed to the production of $N_4{}^+$-e^- pairs by $N_2(B)$-$N_2(B)$ associative ionization.

The values of α_D derived from the data provide confirmation of constants available in the literature and are expected to be of significant benefit in several facets of plasma science and applications, including atmospheric chemistry and simulations predicting and assessing the properties of laser filaments in air [17–19]. In addition to the α_D measurements reported here, an experimental tool designed for measurements of electron density decay rates, in the gas phase and with <5 ns temporal resolution, is introduced.

This article is organized as follows. Section II describes the details concerning the experiments, including the design and performance of the Ti:Al_2O_3-KrF laser system and the microwave interferometer. Extensive testing of the interferometer, including measurements of bandwidth and detection limits, is described and the data acquisition and analysis procedures are discussed. Results of the experiments are presented in Sec. III and compared with rate constants available in the literature, while Secs. IV and V summarize the conclusions of this work.

II. EXPERIMENTAL METHODS AND DATA ACQUISITION

A. Hybrid Ti:Al_2O_3-KrF laser system

Plasma channels were produced in the gas-filled arm of a microwave interferometer with the laser system shown schematically in Fig. 1. A mode-locked Ti:Al_2O_3 (sapphire) oscillator, pumped by a 5 W Nd:YAG laser (532 nm), was tuned to 744 nm where it produced 2.7 nJ, 85 fs pulses at a repetition frequency of 90 MHz. Subsequent amplification of selected pulses in a Ti:sapphire regenerative amplifier driven by a 7 W Nd:$YLiF_4$ laser (512 nm) resulted in a train of 400 μJ seed pulses having a pulse repetition frequency (PRF) of 1 kHz. Diagnostic measurements with a spectrometer, autocorrelator, and frequency-resolved optical gating system show these pulses to have spectral and temporal widths of 25 nm and 160 fs, respectively. Frequency tripling of the seed pulses to 248 nm was accomplished in a three-crystal assembly. After frequency doubling the input radiation in bismuth borate (BiB_3O_6; BIBO), a calcite flat served the dual purpose of rotating the polarization of the second harmonic, and phase matching it with the fundamental. The third harmonic of 744 nm (248 nm) was subsequently generated by sum frequency generation in a β-BaB_2O_4 (BBO) crystal.

Following the tripler, a pulse stretcher comprising a pair of fused silica prisms provided for continuous variation of the laser pulse width over the 500 fs to 2 ps interval. In addition, the stretcher acted as a spectral filter by refracting residual fundamental (744 nm) and second-harmonic radiation out of the beam path and into a trap. After passing through a pinhole filter to remove amplified spontaneous emission (ASE), the pulses were injected into the first of two KrF

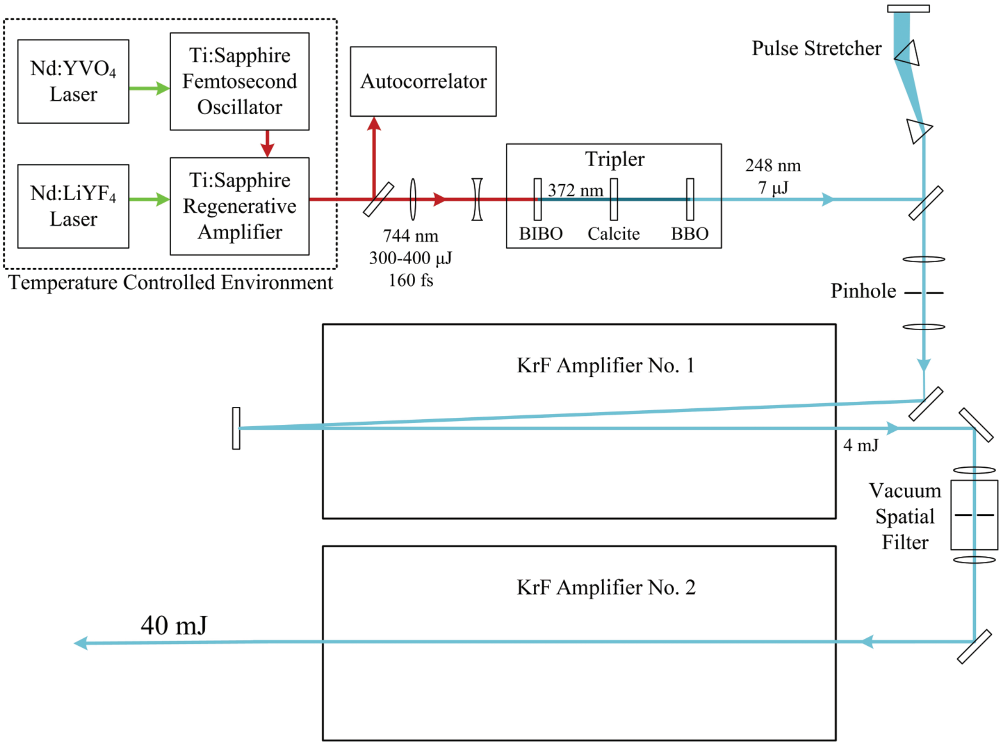

FIG. 1. (Color online) Diagram of the hybrid Ti:sapphire-KrF laser system adopted for generating plasma channels within the microwave interferometer. Producing ~40 mJ, subpicosecond pulses at 248 nm, the system is seeded by ~160 fs pulses at 744 nm, which are subsequently frequency tripled to 248 nm in an assembly comprising bismuth borate (BIBO), calcite, and β-BaB_2O_4 (BBO).

excimer amplifiers and traversed the amplifier twice. Pulses emerging from this first amplifier, having energies of 4 mJ (at a PRF of 10 Hz), entered a vacuum spatial filter, which (like the pinhole filter) again rejects much of the ASE from the deep-ultraviolet laser pulses. A final pass through a second KrF amplifier raises the pulse energies by an order of magnitude to 40 mJ. Autocorrelation of the system output pulses by two photon excitation of ZnSe shows the pulse width (FWHM) to be ~730 fs (sech^2).

Synchronization of the system of Fig. 1 is essential for optimal performance. A photodiode monitoring the output of the Ti:Al_2O_3 oscillator provided an electrical signal that triggered the Pockels cells in the regenerative amplifier and its Q-switched pump. This signal also served ultimately to synchronize the front end of the laser system to the KrF amplifiers. Owing to jitter in the thyratrons driving the two KrF amplifiers, this synchronization procedure was essential for maintaining full power of the system over a period of several hours. Two optical signal waveforms, recorded by monitoring the output pulses from the full system through a dielectric mirror having a transmission of 2%, are shown in Fig. 2. The red trace in the figure represents a laser pulse generated when the timing of the injected (seed) pulse coincides with the point at which peak gain is reached in the amplifiers. When the arrival of the seed pulse is delayed with respect to peak amplifier gain, output pulses having the temporal profile indicated by the black trace are obtained. However, because of the limited bandwidth of the detection system with which the data of Fig. 2 were recorded, the output pulses from the laser system are considerably shorter (<1 ps, as discussed earlier) than is suggested by the waveforms. Also, the double peak following the primary pulse is the result of the amplification of back reflections from windows on the KrF amplifiers.

The maximum intensities of both waveforms in Fig. 2 are normalized, and it should be noted that temporal misalignment of the system results in a loss of at least 50% in pulse energy.

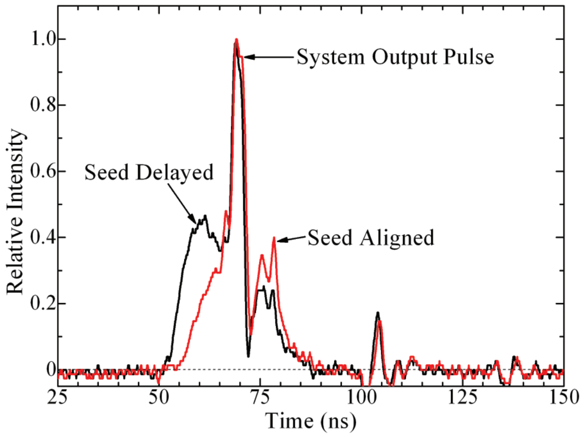

FIG. 2. (Color online) Normalized optical waveforms illustrating the temporal alignment of the Ti:Al_2O_3 seed pulse with the excimer amplifiers (red trace), and a misaligned pulse (black trace). Both pulses were viewed through a dielectric mirror having 2% transmission at 248 nm. Because the bandwidth of the detection system with which these data were recorded is limited to <500 MHz, the temporal width of the laser system output pulses is considerably smaller than that suggested by the waveforms.

When the pulses exiting the second amplifier are focused into laboratory air with a 1.5 m focal length concave mirror, plasma channels (filaments) are clearly visible and extend ~0.5 m on either side of the focal point.

B. Microwave interferometer: Operation, calibration, and bandwidth

Microwave interferometric measurements of electron density in low-temperature plasmas have their origin in experiments [20,21] in which a plasma-induced shift in the resonant frequency of a microwave cavity, or the impedance of a transmission line, was detected. Goldstein *et al.* [22,23]. subsequently extended these results and reported the approach that has since served as the basis of microwave (and laser) interferometry. By propagating a 3–10 GHz signal through plasma within a waveguide and measuring the resulting attenuation and phase shift of the incident wave, they were able to measure both the electron density and collision frequency of the plasma.

Figure 3 is a diagram (not to scale) of the microwave interferometer adopted for the present experiments. Similar to systems applied previously to measurements of absolute cross sections for the photoionization of electronically excited molecules or ground-state rare gas atoms [24–27], this X-band interferometer is a full bridge configuration, operating at 9.2 GHz, in which the output of a klystron is split into two beams of equal intensity. One of these propagates through the arm in which plasma channels are produced, whereas the other half of the klystron power traverses the reference arm of the interferometer, which comprises a variable attenuator and a phase shifter. Both the attenuator and phase shifter were fitted with stepper motors and calibrated potentiometers so as to enable computer control and readout of the system. By adjusting the attenuator and phase shifter, both arms of the interferometer could be balanced prior to introducing plasma into the experimental arm. The two arms of the interferometer terminate at a magic-tee junction, which provides electrical outputs corresponding to the sum (Σ) and difference (Δ) of the signals arriving from both arms of the system. This capability enables the amplitude and phase of the signal emerging from the measurement arm of the interferometer, relative to that for the reference arm, to be monitored in real time. Plasma channels (or filaments) are produced in a 100 cm length of rectangular X-band waveguide that contains Ar or N_2 at the desired pressure. Polytetrafluoroethylene [PTFE (Teflon)] windows installed within the waveguide (but outside the plasma region) provided a vacuum seal to isolate the experimental and reference arms of the interferometer. Glass was chosen initially for this vacuum barrier but its reflectivity at 9.2 GHz (~50%) is prohibitive, and PTFE was found to have negligible insertion loss. The subpicosecond laser pulses entered and exited the experimental arm of the interferometer through ~9-mm-diam. holes produced in E-bend sections of waveguide. In order to avoid damage to the window admitting the ~80 GW pulses to the interferometer, ultraviolet-grade fused silica windows were sealed to sections of stainless steel tubing, ~90 cm in length, which in turn were welded to the waveguide bends on each side of the experimental arm. The entire experimental arm of the interferometer (including the 90 cm extensions)

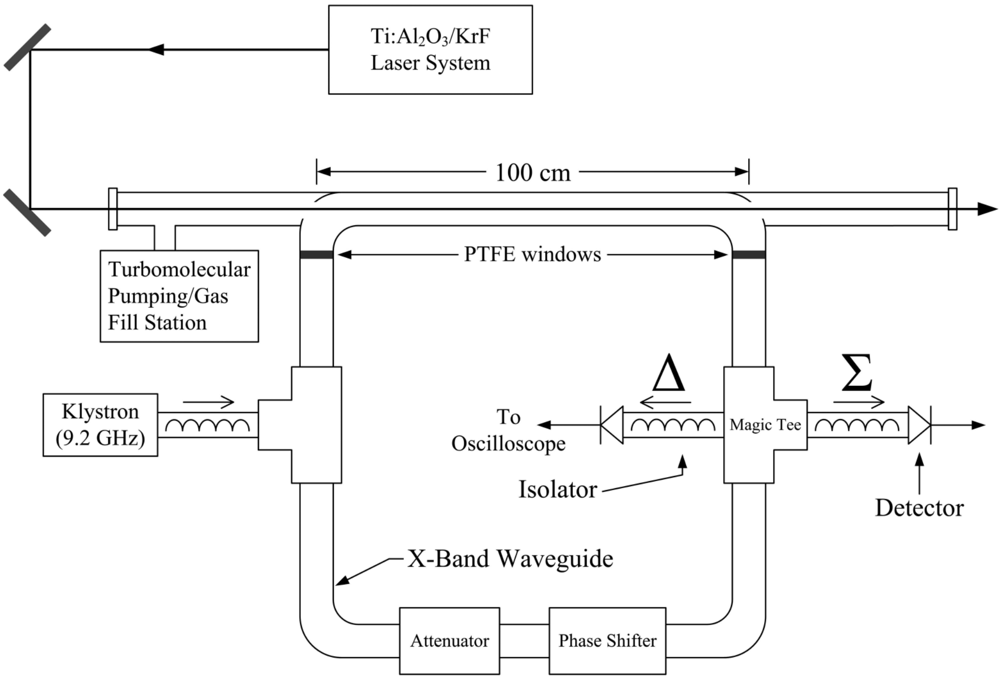

FIG. 3. Diagram (not to scale) of the full bridge microwave interferometer, operating at 9.2 GHz. PTFE is an acronym representing polytetrafluoroethylene (Teflon), and the lower half of the interferometer is its reference arm.

was evacuated by a turbomolecular pump to $\leqslant 10^{-5}$ Torr and back-filled to the desired pressure of research-grade Ar or N_2.

Obtaining meaningful and reproducible data from an interferometer requires calibration of the components and the microwave diode detectors (Fig. 3), specifically. Accordingly, calibration curves were obtained for each diode with a microwave circuit designed to measure the nonlinear response of the two (or more) diodes of Fig. 3 separately but simultaneously. Of equal importance in experiments of the nature reported here is the frequency response of the individual components of the interferometer. Interpreting short-time-scale transients in the temporal decay of the electron density, in particular, is dependent upon the overall bandwidth of the bridge. A microwave circuit developed to test interferometer components demonstrated that the magic tee sets the limit on the frequency response of the system. Figure 4 is a diagram of a circuit arranged specifically for probing a magic tee and measuring its bandwidth. To simulate a high-speed input signal, two klystrons (tuned to frequencies differing by as much as 900 MHz) provide a beat signal at the magic tee under test. Spectral domain representations [Fast Fourier Transforms (FFTs)] of the signals transmitted by the magic tees showed fidelity of the output to the input signal for beat frequencies up to 600 MHz (klystron 1: 9.5 GHz; klystron 2:10.1 GHz) but clear distortion of the waveform for input beat frequencies beyond 800 MHz.

Measurements with the microwave detectors and a digital signal analyzer having >8 GHz bandwidth showed the response of these components to extend to at least the nominal microwave carrier frequency of 9.2 GHz. We conclude, therefore, that the bandwidth of the interferometer of Fig. 3 is limited by the magic tee to frequencies slightly below 800 MHz. For all of the data presented in Sec. IV, the temporal history of the signals appearing at the sum (Σ) and difference (Δ) ports of the magic tee was detected with a 1 GHz bandwidth oscilloscope.

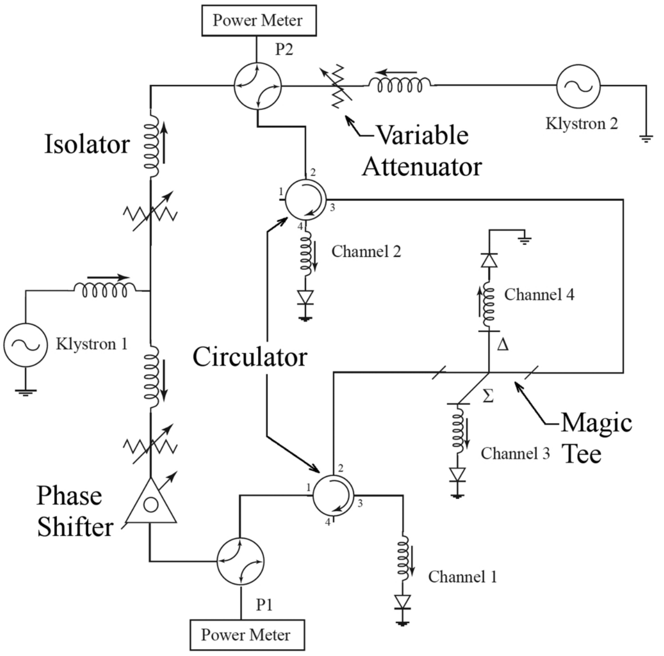

FIG. 4. Microwave circuit developed to determine the frequency response of the magic tees (and other interferometer components) of Fig. 3. Having two klystrons operating at frequencies differing by no more than 900 MHz, this arrangement facilitated the measurement of component bandwidths to ~1 GHz.

III. THEORETICAL CONSIDERATIONS AND DATA ACQUISITION

Because the theory underlying the operation of microwave (and laser) interferometers has been discussed in detail previously [24–27], only the highlights will be reviewed here. Briefly, the magnitude of the complex propagation constant $\gamma = \alpha + i\beta$, for an electromagnetic wave propagating in a waveguide partially filled with plasma, is given by

$$\gamma^2 - \gamma_0^2 = i\omega\mu_0 \frac{\iint \mathbf{E}_0 \cdot \mathbf{J}\, dA}{\iint \mathbf{E}_0 \cdot \mathbf{E}\, dA}, \tag{2}$$

where γ_0 and $\mathbf{E}_0$ are the propagation constant and the electric field in the empty waveguide, respectively, $\mathbf{E}$ is the electric field in the presence of the plasma, ω is the radian frequency of the electromagnetic wave, and $\mathbf{J}$ is the current density. For collisional plasmas, $\mathbf{J}$ is expressed as

$$\mathbf{J} = \sigma\mathbf{E} = \frac{ne^2}{m_e}\frac{\nu_m - i\omega}{\nu_m^2 + \omega^2}\mathbf{E}, \tag{3}$$

where m_e is the electron mass, n is the electron number density, and ν_m is the collision frequency for momentum transfer. Since the electron density varies spatially, it must remain within the integrand of Eq. (2) which can be written

$$\gamma^2 + \beta_0^2 = i\omega\mu_0 \frac{e^2}{m_e}\frac{\nu_m - i\omega}{\nu_m^2 + \omega^2}\frac{\iint n\mathbf{E}_0 \cdot \mathbf{E}\, dA}{\iint \mathbf{E}_0 \cdot \mathbf{E}\, dA}, \tag{4}$$

where $\gamma_0 \equiv i\beta_0$ for an evacuated waveguide. If $\nu_m \ll \omega$, then Eq. (4) becomes

$$\alpha^2 - \beta^2 + \beta_0^2 + 2i\alpha\beta = (\omega - i\nu_m)\frac{\mu_0 e^2}{m_e \omega}\frac{\iint n\mathbf{E}_0 \cdot \mathbf{E}\, dA}{\iint \mathbf{E}_0 \cdot \mathbf{E}\, dA}. \tag{5}$$

For simplicity, the spatial dependence of the electron density is described by the relation $n = n_e f(x,y)$, where *f(x,y)* represents the spatial distribution of the plasma density in the plane transverse to the direction of propagation of the microwave or optical field. Assuming $\mathbf{E} \approx \mathbf{E}_0$, we define the filling factor F as

$$F = \frac{\iint f(x,y)\mathbf{E}_0^2\, dA}{\iint \mathbf{E}_0^2\, dA}. \tag{6}$$

Separating Eq. (5) into its real and imaginary components yields

$$\alpha^2 - \beta^2 + \beta_0^2 = \frac{\omega_p}{c^2}F \tag{7}$$

and

$$2\alpha\beta = \frac{\omega_p}{c^2}\frac{\nu_m}{\omega}F, \tag{8}$$

where the plasma frequency $\omega_p = n_e e^2/m_e\varepsilon_0$. The plasma propagation constants α and β are related to the phase shift $\Delta\varphi$ and attenuation a measured by the interferometer for a given value of n_e. Specifically,

$$\beta = \beta_0 - \frac{\Delta\varphi}{L}, \tag{9}$$

where β_0, the vacuum propagation constant (determined by the waveguide cross section), is 1.35 cm^{-1} for the present experiments, $\Delta\varphi$ is expressed in radians, and L is the plasma–microwave-field interaction length. On the basis of Eqs. (7) and (9), the spatially averaged electron density can be calculated from the expression

$$n_e = \frac{1}{F}\frac{m_e}{\mu_0 e^2}\left(\alpha^2 - \beta^2 + \beta_0^2\right). \tag{10}$$

The detection floor for the interferometer of Fig. 3 is estimated from Eq. (10) to be $\approx 10^{10}$ cm^{-3} by setting $\alpha = 0$ and assuming L and F to be 1 m and 0.1, respectively. The latter was estimated from a series of measurements of the cross-sectional profile of the 248 nm laser beam along the interferometer's experimental arm.

The Σ port of the magic tee (Fig. 3) provides a signal $[S_\Sigma(t)]$ that is simply the square of the sum of the electric field amplitudes arriving from the reference and experimental arms of the interferometer. That is:

$$S_\Sigma(t) = [E_E(t) + E_R(t)]^2 \tag{11}$$

where $E_E(t)$ and $E_R(t)$ denote the respective field amplitudes at the magic-tee input port at time t. In contrast, the Δ port also sums $E_E(t)$ and $E_R(t)$ but introduces a phase shift of π (and, therefore, $S_\Delta(t) = [E_E(t)–E_R(t)]^2$). Consequently, if the electric field amplitudes in the reference and experimental arms at any time t are represented by the expressions $E_R(t) = A_R\,\sin(\omega t)$ and $E_E(t) = A_E(t)\cos[\omega t + \delta(t)]$, then it can be shown that the phase shift $\delta(t)$ can be determined from the relation

$$\sin\delta(t) = \frac{S_\Delta(t) - S_\Sigma(t)}{4A_E(t)A_R}, \tag{12}$$

where A_R is a constant. Similarly,

$$A_E^2(t) = \frac{S_\Delta(t) + S_\Sigma(t)}{2} - A_R^2 \tag{13}$$

and the attenuation a (expressed in dB) is determined by the expression

$$a(t) = 20\log_{10}\left(\frac{A_E(t)}{A_R}\right). \tag{14}$$

IV. EXPERIMENTAL RESULTS AND DISCUSSION

A. Representative data and analysis

Data representative of those obtained throughout these experiments are presented in Fig. 5. Waveforms recorded at both the Σ and Δ ports of the interferometer (but already corrected for the nonlinear response of the microwave diodes) are shown on the $0 \leqslant t \leqslant 30$ μs time scale, where $t = 0$ denotes the arrival of the 248 nm laser pulse at the interferometer. Notice that at $t = 0$ the values of S_Σ and S_Δ are equal because the interferometer is balanced [i.e., the amplitudes A_E and A_R of Eqs. (12) and (13) are equal but the two arms are 90° out of phase] prior to the production of the plasma. From data similar to those of Fig. 5, the temporal histories of the phase shift and attenuation of the microwave probe field can be calculated, and typical results are given in Fig. 6 (for $p_{\mathrm{Ar}} = 300$ Torr). Extracting the electron density from the phase shift and attenuation data requires accounting for the reversal in the sign of $\sin[\delta(t)]$ that is obvious in Fig. 6. Negative values of $\sin[\delta(t)]$ reflect $\delta(t)$ values above

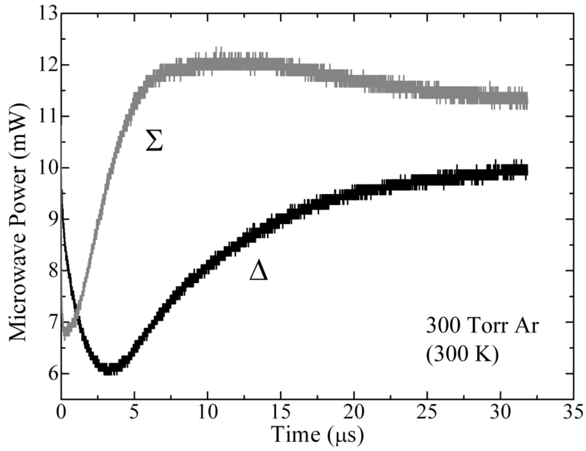

FIG. 5. Waveforms representative of those recorded at the Σ and Δ ports of the interferometer of Fig. 3 when incoming 248 nm laser pulses photoionize Ar. These data were obtained for an Ar pressure (300 K) of 300 Torr.

$\pi/2$, which has the effect of introducing a discontinuity into the $n_e(t)$ profiles when the phase shift momentarily equals $\pi/2$. Compensating for this brief interruption in the calculated electron density entails fitting to the data a polynomial function spanning a small region in time near t' where $\sin[\delta(t')] = \pi/2$.

Before leaving this section, a few comments regarding electron diffusion and its impact on interpreting the experiments are warranted. The loss of electrons to the waveguide walls must be considered because the electron density transients presented in the next two sections extend to 1 μs and beyond. However, solutions of the diffusion equation show such losses to be negligible over the range in Ar or N_2 pressure investigated. For 50 Torr of Ar, for example, <4% of the initial number of photoelectrons produced by the laser have been lost to the waveguide walls at $t = 10$ μs. At $t = 20$ μs, this value remains below 10%. An issue of greater consequence is the change in the filling factor F as electrons diffuse radially outward from the photoionization region. In order to compensate for this effect, the electron density determined at any time t from Eqs. (10) and (12)–(14) is normalized to the calculated value of F at that time.

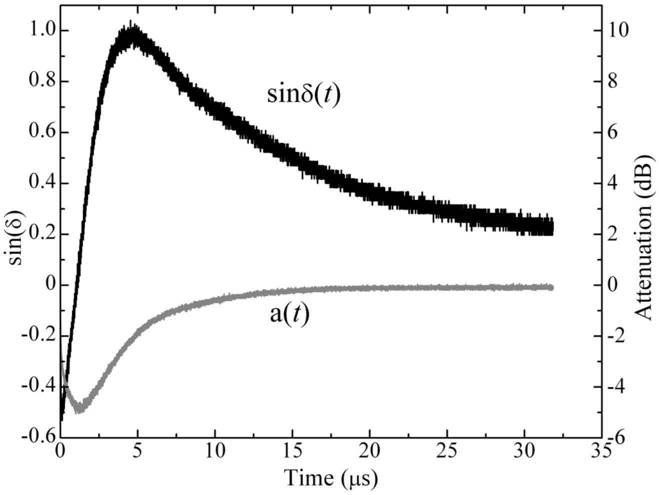

FIG. 6. Phase and attenuation profiles calculated from waveforms similar to those of Fig. 5. The Ar pressure is again 300 Torr.

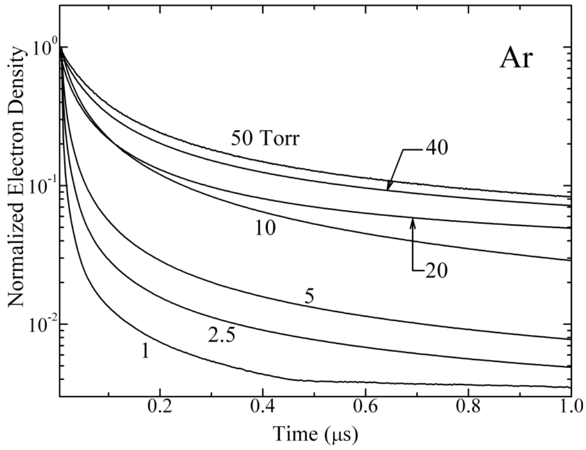

FIG. 7. Normalized electron density decay data acquired at selected Ar pressures between 1 and 50 Torr.

B. Electron decay processes in Ar: Determination of α_D

Argon was chosen for initial study, primarily because of the potential of the present experimental approach in determining rate constants and cross sections that remain unknown or are not well characterized. Production of electrons with subpicosecond laser pulses simplifies data analysis and, specifically, the extraction of electron density decay constants from temporal transients because the deconvolution of the electron density temporal history from the source function is no longer necessary. Another aspect of the motivation for investigating Ar is its role in technological plasmas such as those in lasers, lamps, and semiconductor processing tools.

Data were obtained at pressures ranging from 1 to 650 Torr. For each pressure, the temporal dependence of the electron density was calculated from the phase and attenuation data recorded for every laser shot. Averaging all of the data acquired from multiple (minimum of 20) shots determined the final (composite) profile. Normalized electron density decay curves, obtained for Ar pressures (p_{Ar}) between 1 and 50 Torr, are shown in a semilogarithmic format in Fig. 7. Similar results are presented in Fig. 8 for selected values of p_{Ar} in the 100–500 Torr interval. The data of Figs. 7 and 8 have been corrected for both the microwave detector response and electron diffusion, as discussed earlier. Interpreting the electron density decay data of Figs. 7 and 8 (as well as other data not shown) requires numerical simulations based on a description of the dominant kinetics processes, and Table I summarizes the key mechanisms [12,28–34] that have been incorporated into the model of the present work. Adapted from Ref. [35], the model presumes that optical energy is delivered to the Ar gas primarily through four-photon ionization of the atom which produces an $\mathrm{Ar}^+(^2P_{3/2})$ ion and a ~4.25 eV electron. Dimerization of the atomic ion to form $\mathrm{Ar_2}^+$ in its ground state $(X\,^2\Sigma_u{}^+)$ is followed by dissociative recombination (process no. 3, Table I), an e^--$\mathrm{Ar_2}^+$ interaction that is known to be strongly dependent upon electron temperature T_e and results in a neutral Ar atom residing in an excited state. Three-body formation of the $\mathrm{Ar_2}^*(a\,^3\Sigma_u{}^+)$ excimer species and associative

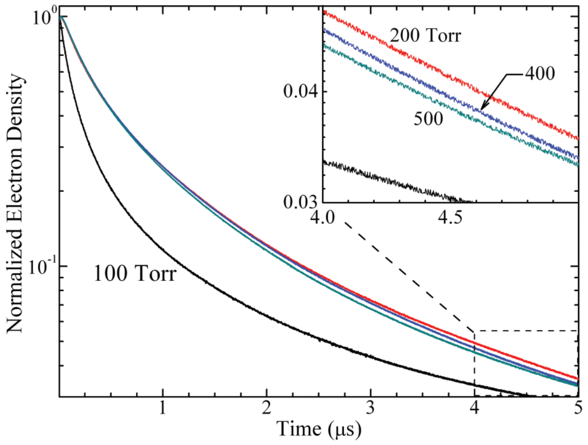

FIG. 8. (Color online) Data similar to those of Fig. 7 but recorded for Ar pressures in the 100–500 Torr interval. Expanded views of the $p_{Ar} = 100$, 200, 400, and 500 Torr curves in the $4 \leqslant t \leqslant 5$ μs region are shown by the inset.

ionization collisions, in which two Ar(4s) metastable atoms yield a dimer ion, are also considered. Although the 4s and 4p manifolds of excited states are specifically identified in Table I, the model considers them (and other atomic states that might be populated) as one. The influence of this assumption on the constants derived from the simulations appears to be small. Additional processes incorporated into the model include radiative decay of the $a\,^3\Sigma_u{}^+$ and $A\,^1\Sigma_u{}^+$ excited states of neutral Ar_2, electron mixing of these states, electron cooling through elastic collisions, and electron impact ionization of both the Ar (4s) and Ar_2 ($a\,^3\Sigma_u{}^+$) metastable species. Several of these reactions are not listed in Table I because their impact on the model predictions is slight.

Because of the known sensitivity of electron-ion recombination rates in the rare gases to the electron temperature T_e, a few comments regarding the rate of cooling of the electrons generated by Ar photoionization are warranted. Although (as noted earlier) photoelectrons in these experiments are born with ∼4.25 eV of energy, electron thermalization through e^-–heavy-particle collisions proceeds rapidly. Calculated from the cross section for momentum transfer in e^--Ar collisions, the rate constant for electron cooling is $\sim 10^9\ \mathrm{s^{-1}\,Torr^{-1}}$ or $\sim 3 \times 10^{-8}\ \mathrm{cm^3\,s^{-1}}$. Since at least 10^4 of such elastic collisions are required to thermalize the initially hot electrons, however, the cooling process requires ∼10 μs for a background gas pressure of 1 Torr but only ∼100 ns when the pressure is 100 Torr. For this reason, virtually all of the results presented in the discussion to follow were obtained at gas pressures above 100 Torr. At lower pressures (such as the $1 \leqslant p_{Ar} \leqslant 50$ Torr data of Fig. 7), the electron energy decays monotonically in time throughout the electron density decay transient and such data can be viewed as a diagnostic of the dependence of α_D on T_e. We conclude that low-pressure data similar to those of Fig. 7 provide a means to observe in real time the interaction of electrons with $Ar_2{}^+$ over a specified range in electron energies. This capability may offer the opportunity, therefore, to observe resonances in the dependence of the e^--ion recombination cross section on electron velocity, and to do so on a time-resolved basis. However, an analysis of the sub-50-Torr data that incorporates time-varying electron energies has not yet been completed and, throughout the remainder of this discussion, the electrons are assumed to be cooled in a time comparable to that required for $Ar_2{}^+$ formation (reaction no. 2, Table I). Thus, the α_D values presented here represent the dissociative recombination rate constants associated with the interaction of a dimer ion with a thermal electron.

The rate constants and cross sections in Table I were the assumed *initial* values for the simulations. Optimizing the fit of the model predictions to the data consisted of two steps, the first of which involved a sensitivity analysis wherein one of the model's rate constants was varied while keeping the others constant. This process identified dissociative recombination and four-photon ionization as the processes on which the model predictions were most dependent. The final step in fitting the model to the data involved a modification of simulated annealing [36], a form of genetic optimization algorithm in which the critical constants are varied simultaneously because their associated rates are interdependent. In the early stages of the optimization algorithm, these constants were varied in steps of ±40% but the process gradually lowered the variations in each to ±10%. Throughout this procedure, the best fit of a calculated electron density profile to experiment was defined in terms of minimizing the weighted sum of residuals between the simulation and the data.

One outcome of the procedure outlined above is that the experimentally determined electron density profiles can be matched over a range in Ar pressure of an order of magnitude. An example of a comparison between experiment and the numerical simulations is provided in Fig. 9 for

TABLE I. Summary of the primary kinetic processes, rate constants, and cross sections adopted for analysis of the electron density decay data for Ar.

Process[a]	Rate constant or cross section[b,c]	Refs.
1. $Ar + 4\hbar\omega \rightarrow Ar^+ + e^-$	$1 \times 10^{-116}\ \mathrm{cm^8\,s^3}$	[28,29]
2. $Ar^+(^2P_{3/2}) + 2Ar \rightarrow Ar_2{}^+(X\,^2\Sigma_u{}^+) + Ar$	$2.5 \times 10^{-31}\ \mathrm{cm^6\,s^{-1}}$	[30]
3. $Ar_2{}^+(X) + e^- \xrightarrow{\alpha_D} Ar^*(4p) + Ar$	$2 \times 10^{-7}\ T_e{}^{-0.67}\ \mathrm{cm^3\,s^{-1}}$	[12]
4. $2Ar^*(4s) \rightarrow Ar_2{}^+(X) + e^-$	$5 \times 10^{-10}\ \mathrm{cm^3\,s^{-1}}$	[31–33]
5. $Ar^*(4s) + 2Ar \rightarrow Ar_2^*(a\,^3\Sigma_u{}^+) + Ar$	$1 \times 10^{-32}\ \mathrm{cm^6\,s^{-1}}$	[34]

[a] An asterisk denotes an electronically excited species.
[b] Electron temperature T_e is expressed in eV.
[c] The values indicated are those adopted for the initial simulations.

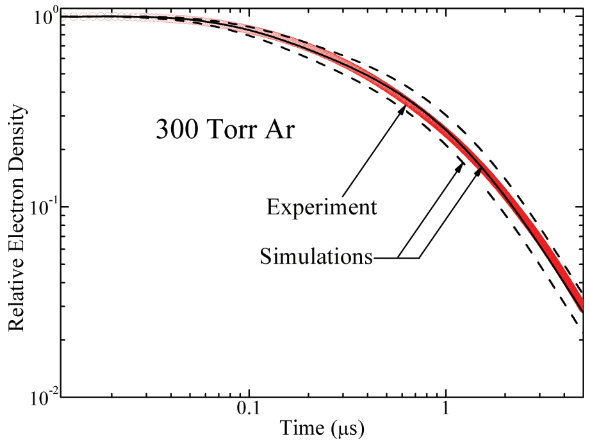

FIG. 9. (Color online) Comparison of experimental measurements (red circles) of the normalized, time-dependent electron density with numerical simulations. The solid black curve represents the optimal fit of the model of Table I to the data, and the dashed curves illustrate the results obtained by varying the constants (discussed in the text) from their optimal values by no more than 20%.

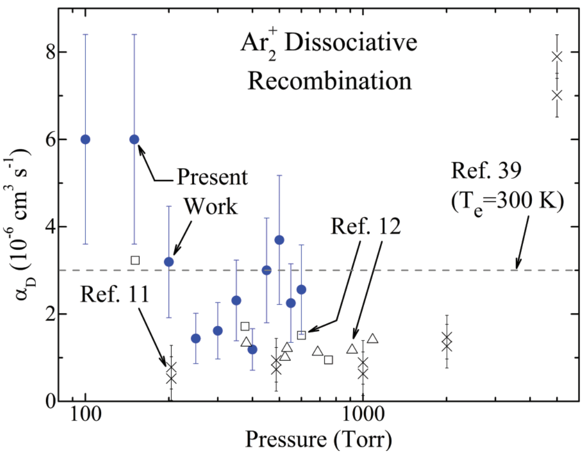

FIG. 10. (Color online) Summary of the measurements available in the literature for α_D, the rate coefficient for the dissociative recombination of Ar_2^+, in the $100 \leqslant p_{Ar} \leqslant 5000$ Torr interval. Constants reported in Refs. [11,12] are compared with those of the present work. One theoretical value from Ref. [39] (for $T_e = 300$ K) is also shown. The results of Cooper *et al.* [12] are divided into two groups, one of which (open triangles) represents the addition of 4 Torr of He to the indicated pressure of Ar in order to effect the rapid thermalization of electrons. The estimated uncertainty of ±40% is also indicated by the error bars for each of the measurements reported here.

$p_{Ar} = 300$ Torr. Data are indicated by the red circles, and the solid black curve illustrates the optimized fit of the model of Table I to the experimental profile. As one indication of the sensitivity of the optimization procedure to the derived constants, the dashed curves in Fig. 9 represent two worst-case (*maximized* weighted residuals sum) predictions generated when the constants (or rates) mentioned above are varied from their optimum values by no more than 20%. Extensive simulations of electron density temporal profiles (similar to those of Figs. 7–9) demonstrated that α_D, the rate constant for dissociative recombination of $Ar_2^+(X)$, and the cross section for four-photon ionization of $Ar(3p^6\,{}^1S_0)$ at 248 nm could be isolated and determined. For the other rate constants incorporated into the model, simulations were either insensitive to the value of a specific parameter or they yielded values quite close to those available from the literature. For example, the electron thermalization rate constant extracted from numerical simulations of the 150–600 Torr Ar data is $(4.3 \pm 1.5) \times 10^{-8}$ cm^3 s^{-1}, which is in agreement with values calculated from the e^--Ar cross section for momentum transfer (3×10^{-8} cm^3 s^{-1}).

1. Dissociative recombination of $Ar_2^+(X\,{}^2\Sigma_u^+)$

As discussed briefly in the Introduction, dissociative recombination was identified in 1963 by Biondi [2] as the dominant electron loss mechanism in low-temperature plasmas produced in the heavier rare gases (Ne, Ar,...). The now-accepted temperature dependence of α_D was measured to be $T_e^{-0.67}$ by Mehr and Biondi [37] in 1968 and, a decade later, Shiu and Biondi [38] reported fluorescence measurements designed to assess the Ar* product state distribution resulting from the process. All of these measurements were made at low pressures (1–50 Torr) and since 1978 only two additional experiments have been reported. Both Kuo and Keto [11] and Cooper *et al.* [12] employed electron beam excitation of Ar at pressures above 100 Torr to estimate α_D. The former group [11] detected Ar(4p) optical emission as a diagnostic of the dissociative recombination process, whereas an ac microwave conductivity measurement was adopted in Ref. [12] to monitor directly the decay of the electron density.

Figure 10 compares the data of Refs. [11,12] with the results of the present work in the 100–650 Torr pressure interval. The rate constants obtained from the experiments and simulations described earlier are represented by the solid dots, and the estimated uncertainty (±40%) associated with the measurements at each pressure is indicated. Two sets of data are shown for Cooper *et al.* [12] who obtained values for α_D with and without the presence of 4 Torr of He (open triangles and squares, respectively, of Fig. 10), added to Ar for the purpose of accelerating the thermalization of the electrons. The values of α_D derived from the present experiments span a range in pressure in which few data have been available in the past. However, these results are consistent with prior work; for example, the values between 100 and 200 Torr in Fig. 10 appear to confirm a rise in α_D below 200 Torr, as suggested by the Ref. [12] measurement at 150 Torr. Similarly, the present measurements of α_D in the 200–650 Torr range are in general agreement with the values of Refs. [11,12], particularly for $250 \leqslant p_{Ar} \leqslant 400$ Torr. A sampling of the theoretical predictions of Royal and Orel [39] is also given in Fig. 10. Because of the rapid thermalization of the electrons that is reflected in the high-Ar-pressure data of Fig. 10, the value of α_D calculated in Ref. [39] for $T_e = 300$ K ($\sim 3 \times 10^{-7}$ cm^3 s^{-1}) was chosen for comparison.

As indicated in Fig. 10, the rate constants reported here were determined at pressures spanning the gap between early, low-pressure experiments (in which the plasma was generally produced by microwave breakdown) and the electron beam excitation studies of Refs. [11,12]. A thorough review of the experimental measurements of α_D reported prior to 1983 can be found in Ref. [12]. The present values of α_D are in general agreement with both experiment and theory [39]. However, a statistically significant rise in α_D is observed for $p_{Ar} >$ 400 Torr, which appears to contrast with the invariance of the data of Refs. [11,12] to pressure in the 200–2000 Torr interval. Additional measurements at higher Ar pressures will be required to determine if this trend in α_D persists with further increases in p_{Ar}, possibly reflecting the onset of three-body recombination processes [11].

2. *Four-photon ionization of Ar ($3p^6\ ^1S_0$)*

Absolute cross sections for the photoionization of atoms or small molecules in the ground, or an excited, state are sparse in the literature, owing to the difficulty in measuring the electron density in a nonperturbative manner. McCown and co-workers [24] measured in 1982 the cross section associated with two-photon ionization of Xe at 193 nm, and Geohegan *et al.* [27] later extended the microwave bridge experiments to investigating two-photon resonant, three-photon ionization of ground-state Kr at 193 nm and 248 nm. More recently, generalized cross sections for the multiphoton ionization of each of the rare gases at 248 nm were determined by Uiterwaal *et al.* [28] from measurements of the ponderomotive shift of above-threshold ionization (ATI) spectra. The value reported in Ref. [28] for Ar, $\sigma^{(4)} = 1.3 \times 10^{-116}$ $cm^8\,s^3$, is approximately one order of magnitude smaller than the cross section (1.9×10^{-115} $cm^8\,s^3$) calculated by van der Hart [40] for an intensity of 10^{13} $W\,cm^{-2}$.

On the basis of the data of Figs. 7 and 8, $\sigma^{(4)}$ is found to be $(5 \pm 3) \times 10^{-118}$ $cm^8\,s^3$, or a factor of 26 below the value of Ref. [28]. Determining $\sigma^{(4)}$ more precisely is not possible with the current experiment, primarily because pulse-to-pulse jitter in the firing of the thyratrons that power the KrF amplifiers introduces an amplitude stability of ±10% in the output pulse energy of the laser system. Despite this limitation, one may conclude that the four-photon ionization cross section measured for Ar in the present experiments is at least an order of magnitude smaller than the only other experimental value in the literature [28].

C. Dissociative recombination of N_4^+

Experiments virtually identical to those described earlier for Ar were also conducted with N_2 and representative measurements of the temporal decay of the normalized electron density are shown in Figs. 11 and 12 for several pressures between 1 and 400 Torr. In order to evaluate these data, a simplified kinetics model (analogous to that of Table I, and condensed primarily from those of Refs. [41–43]) was developed. Although models of nitrogen plasmas can be quite complex, comprising literally hundreds of reactions, relatively few processes are responsible for control of the electron generation and loss rates. Of particular importance are the dimerization of N_2^+ to form N_4^+:

$$N_2^+ + 2N_2(X) \rightarrow N_4^+ + N_2(X), \tag{15}$$

dissociative recombination of the ion:

$$N_4^+ + e^- \rightarrow N_2(B) + N_2(X), \tag{16}$$

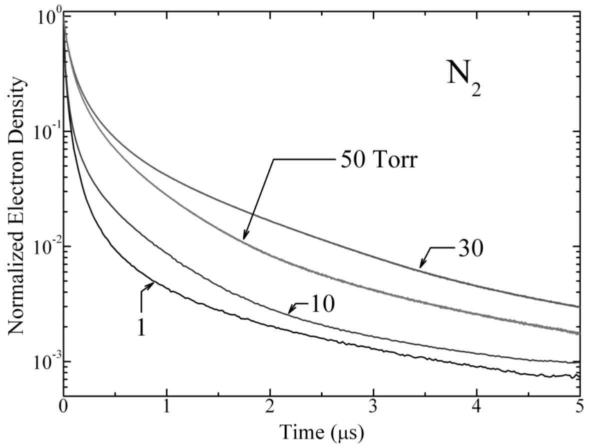

FIG. 11. Temporal decay of the normalized electron density measured for several N_2 pressures (300 K values) between 1 and 50 Torr.

and associative ionization as a result of the collision of two electronically excited dimers:

$$2N_2(B,C) \rightarrow N_4^+ + e^-, \tag{17}$$

where the $B\,^3\Pi_g$, $C\,^3\Pi_u$, and $X\,^1\Sigma_g^+$ (ground) electronic states are noted explicitly in the above reactions, and the $B\,^3\Pi_g$ and $C\,^3\Pi_u$ excited states of N_2 are treated in the simulations as effectively one energy level. Other processes incorporated into the model included (i) energy pooling between two $N_2(A\,^3\Sigma_u^+)$ metastable molecules to produce $N_2(B)$, (ii) associative ionization involving two $N(3s\ ^2P,\ ^4P)$ atoms to yield an N_2^+ ion, and (iii) excitation transfer between the A and B states of N_2 in heavy-particle collisions. The rate constants for these reactions, as well as those of Eqs. (15)–(17), were adopted from Refs. [41,42]. A detailed analysis of the sensitivity of the model's predictions to variations in process rate constants showed that excitation transfer collisions between electronically excited and ground-state nitrogen atoms or N_2 had little impact on the electron density decay rate at any pressure. Similarly, associative ionization of two $N(3s\ ^2P,\ ^4P)$ atoms—producing an N_2^+ ion—was found to have negligible influence on the electron density.

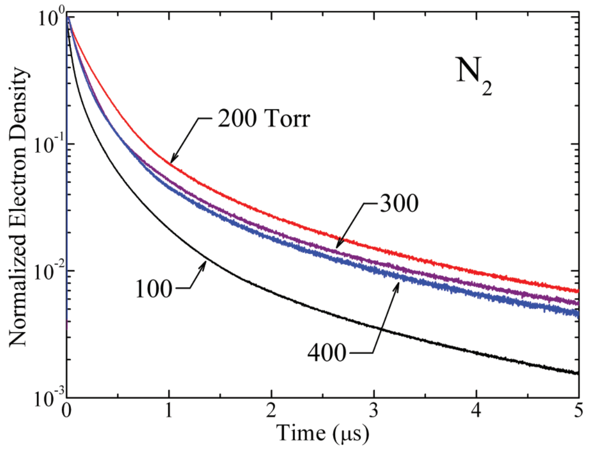

FIG. 12. (Color online) Data similar to those of Fig. 11 for N_2 pressures in the 100–400 Torr range.

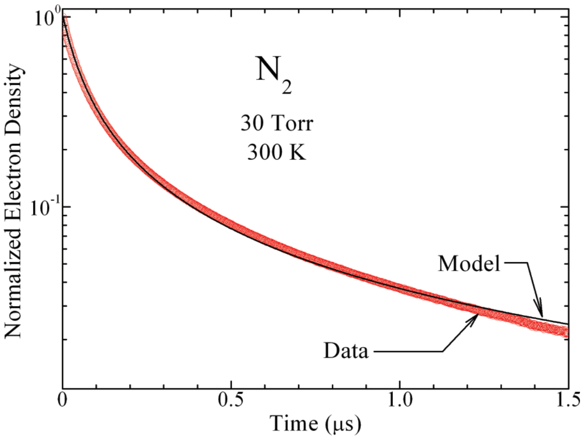

FIG. 13. (Color online) Comparison of experimental electron density decay data (red circles) with the optimized model predictions (black curve) for 30 Torr of N_2.

Modeling of the transients of Figs. 11 and 12 with the aforementioned model was largely successful. As an example, Figs. 13 and 14 compare the experimental data for an N_2 pressure of 30 Torr with the prediction of the model when the rate constant (α_D) for process (16) is taken to be 3.2×10^{-6} $cm^3\,s^{-1}$. At this pressure and others below ~100 Torr, the model was able to reproduce the temporal decay of the electron density quite well, except for t beyond ~1.3 μs where the simulations predict electron density decay rates that are slower than those observed experimentally. An expanded view of the data and model curves of Fig. 13 in the $t < 200$ ns region is presented in Fig. 14. Furthermore, at higher pressures the electron density no longer decays monotonically. As exhibited by the 300 Torr N_2 data presented in Fig. 15, the transient production of supplemental electrons is observed for tens of nanoseconds after the 248 nm laser pulse has exited the interferometer. Because the magnitude of this additional electron generation process peaks <20 ns following the termination of the optical field, and the behavior of Fig. 15 is not present at lower pressures, the process responsible for the momentary increase in electron density appears to be the $N_2(B,C)$-$N_2(B,C)$ associative ionization process of Eq. (17) in which $N_2(B)$ plays a dominant role. In support of this conclusion, we note that the radiative lifetimes of the N_2 C and B states are ~27–44 ns and 9.1 μs, respectively [44]. The failure of the simulations to predict the sub-50-ns transients of Fig. 15 and all high-pressure (>100 Torr) data suggests that the rate constant for the associative ionization process of Eq. (17) is almost an order of magnitude larger than the currently accepted value (5×10^{-11} $cm^3\,s^{-1}$).

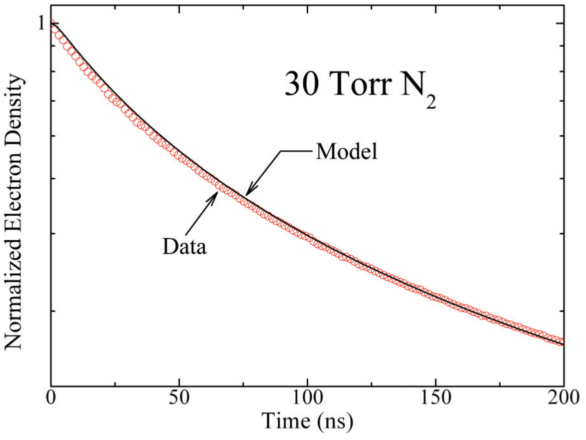

FIG. 14. (Color online) Magnified view of the $t \leqslant 200$ ns portion of the data and model prediction of Fig. 13 ($p_{N2} = 30$ Torr).

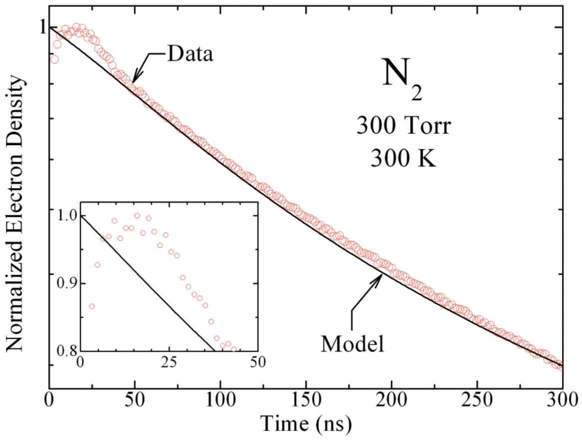

FIG. 15. (Color online) Data and model prediction for 300 Torr of N_2 in the $0 \leqslant t \leqslant 300$ ns time interval. The inset provides an expanded view of the data for $t \leqslant 50$ ns. Note that the ordinate for the full graph is logarithmic while that for the inset is linear.

The dissociative recombination rate constant that represents the best fit of the calculated electron density transients to the data over the entire 10–400 Torr N_2 pressure interval is $(2 \pm 1) \times 10^{-6}$ $cm^3\,s^{-1}$. Although fewer constants exist in the literature for $N_4{}^+$ than was the case with $Ar_2{}^+$ discussed earlier, this result agrees well with values of α_D measured previously in different pressure ranges and with other experimental techniques. At higher pressures, for example, α_D was measured in electron beam excitation experiments to be $(3 \pm 0.6) \times 10^{-6}$ $cm^3\,s^{-1}$ and $(4.6 \pm 0.9) \times 10^{-6}$ $cm^3\,s^{-1}$ for N_2 pressures in the 280–980 Torr and 760–1315 Torr ranges, respectively [13,14]. All other previous work has explored the pressure region below 10 Torr of N_2 but α_D values again range from 1.4×10^{-6} $cm^3\,s^{-1}$ [45] to 2.6×10^{-6} $cm^3\,s^{-1}$ [46]. Thus, the experimental results reported here span the 10–400 Torr gap left by prior experiments. The data and simulations verify that α_D does not (to within experimental uncertainty) change although the N_2 number density has been varied over a range of more than three orders of magnitude.

V. SUMMARY AND CONCLUSIONS

Measurements of the rate constants for the dissociative recombination of $Ar_2{}^+$ and $N_4{}^+$ in 150–600 Torr and 10–400 Torr of background Ar or N_2, respectively, have been reported here. Combining subpicosecond, 40 mJ laser pulses ($\lambda = 248$ nm) as the noninvasive ionization source with microwave interferometry allows for the temporal history of the absolute photoelectron number density to be determined without deconvolving the source function from the observed transients. Although calibration of every component of the interferometer found the system bandwidth to be limited to ~800 MHz, this frequency response is ample to observe sub-50-ns transients in the temporal history of the electron density in N_2 that are attributed to the production of N_4^+-e^- pairs by $N_2(B)$-$N_2(B)$ associative ionization. Values of α_D determined through comparisons of the electron density temporal decay with numerical models yield constants [$(1-6)\times10^{-6}$ cm^3 s^{-1} for Ar_2^+, $(2\pm1)\times10^{-6}$ cm^3 s^{-1} for N_4^+] that are consistent with values measured previously in different gas pressure ranges and with other experimental approaches. Decoupling *in situ* electron production with a subpicosecond, deep-ultraviolet laser from the noninvasive detection of electrons by interferometry allows for electron loss processes to be observed in real time and on the <10 ns time scale. The application of this experimental approach to the investigation of the recombination of molecular ions in chemically aggressive or strongly attaching environments appears to be particularly promising.

ACKNOWLEDGMENT

The support of this work by the U.S. Air Force Office of Scientific Research under Grant No. FA9550-10-1-0048 is gratefully acknowledged.

[1] C. Kenty, Phys. Rev. **32**, 624 (1928).
[2] M. A. Biondi, Phys. Rev. **129**, 1181 (1963).
[3] M. A. Biondi and S. C. Brown, Phys. Rev. **76**, 1697 (1949).
[4] M. A. Biondi, Phys. Rev. **83**, 1078 (1951).
[5] A. Redfield and R. B. Holt, Phys. Rev. **82**, 874 (1951).
[6] M. C. Sexton and J. D. Craggs, Electronics and Control **4**, 493 (1958).
[7] H. J. Oskam and V. R. Mittelstadt, Phys. Rev. **132**, 1445 (1963).
[8] J. N. Fox and R. M. Hobson, Phys. Rev. Lett. **17**, 161 (1966).
[9] M. Ohwa, T. J. Moratz, and M. J. Kushner, J. Appl. Phys. **66**, 5131 (1989).
[10] B. Lay, R. S. Moss, S. Rauf, and M. J. Kushner, Plasma Sources Sci. Technol. **12**, 8 (2003).
[11] C.-Y. Kuo and J. W. Keto, J. Chem. Phys. **78**, 1851 (1983).
[12] R. Cooper, R. J. van Sonsbeek, and R. N. Bhave, J. Chem. Phys. **98**, 383 (1993).
[13] M. C. Sauer and W. A. Mulac, J. Chem. Phys. **56**, 4995 (1972).
[14] Y. Ikezoe, S. Matsuoka, and H. Nakamura, Chem. Phys. Lett. **177**, 366 (1991).
[15] R. A. Phaneuf, C. C. Havener, G. H. Dunn, and A. Müller, Rep. Prog. Phys. **62**, 1143 (1999).
[16] D. Auerbach, R. Cacak, R. Caudano, T. D. Gaily, C. J. Keyser, J. W. McGowan, J. B. A. Mitchell, and S. F. J. Wilk, J. Phys. B **10**, 3797 (1977).
[17] A. Braun, G. Korn, X. Liu, D. Du, J. Squier, and G. Mourou, Opt. Lett. **20**, 73 (1995).
[18] S. Tzortzakis, M. A. Franco, Y.-B. André, A. Chiron, B. Lamouroux, B. S. Prade, and A. Mysyrowicz, Phys. Rev. E **60**, R3505 (1999).
[19] G. Rodriguez, A. R. Valenzuela, B. Yellampalle, M. J. Schmitt, and K.-Y. Kim, J. Opt. Soc. Am. B **25**, 1988 (2008).
[20] D. J. Rose, D. E. Kerr, M. A. Biondi, E. Everhart, and S. C. Brown, Research Laboratory of Electronics, MIT, Technical Report No. 140, 1949 (Cambridge, MA, unpublished).
[21] R. E. B. Markinson, P. C. Thonemann, R. B. King, and J. V. Ramsay, Proc. Phys. Soc., London, Sect. B **64**, 665 (1951).
[22] L. Goldstein, M. A. Lampert, and R. H. Geiger, Electron. Commun. **29**, 243 (1952).
[23] L. Goldstein, in *Advances in Electronics and Electron Physics*, edited by L. Marton (Elsevier, The Netherlands, 1955), Vol. VII, pp. 399–503.
[24] A. W. McCown, M. N. Ediger, and J. G. Eden, Phys. Rev. A **26**, 3318 (1982).
[25] A. W. McCown, M. N. Ediger, and J. G. Eden, Phys. Rev. A **29**, 2611 (1984).
[26] D. B. Geohegan, A. W. McCown, and J. G. Eden, J. Chem. Phys. **81**, 5336 (1984).
[27] D. B. Geohegan, A. W. McCown, and J. G. Eden, Phys. Rev. A **33**, 269 (1986).
[28] C. J. G. J. Uiterwaal, D. Xenakis, D. Charalambidis, P. Maragakis, H. Schroder, and P. Lambropoulos, Phys. Rev. A **57**, 392 (1998).
[29] X. Guan, C. J. Noble, O. Zatsarinny, K. Bartschat, and B. I. Schneider, Phys. Rev. A **78**, 053402 (2008).
[30] B. E. Cherrington, *Gaseous Electronics and Gas Lasers* (Pergamon, Oxford, 1979).
[31] E. Zamir, C. W. Werner, W. P. Lapatovich, and E. V. George, Appl. Phys. Lett. **27**, 56 (1975).
[32] H. Brunet, B. Lacour, J. Rocca Serra, M. Legentil, S. Mizzi, S. Pasquiers, and V. Puech, J. Appl. Phys. **68**, 4474 (1990).
[33] V. A. Ivanov, Sov. Phys. Usp. **35**, 17 (1992).
[34] T. Oka, M. Kogoma, M. Imamura, S. Arai, and T. Watanabe, J. Chem. Phys. **70**, 3384 (1979).
[35] S. Neeser, T. Kunz, and H. Langhoff, J. Phys. D: Appl. Phys. **30**, 1489 (1997).
[36] S. Kirkpatrick, C. D. Gelatt, and M. P. Vecchi, Science **220**, 671 (1983).
[37] F. J. Mehr and M. A. Biondi, Phys. Rev. **176**, 322 (1968).
[38] Y. J. Shiu and M. A. Biondi, Phys. Rev. A **17**, 868 (1978).
[39] J. Royal and A. E. Orel, Phys. Rev. A **73**, 042706 (2006).
[40] H. W. van der Hart, Phys. Rev. A **73**, 023417 (2006).
[41] I. A. Kossyi, A. Yu. Kostinsky, A. A. Matveyev, and V. P. Silakov, Plasma Sources Sci. Technol. **1**, 207 (1992).
[42] N. Popov, Plasma Phys. Rep. **35**, 436 (2009).
[43] H. Brunet and J. Rocca-Serra, J. Appl. Phys. **57**, 1574 (1985).
[44] H. Okabe, *Photochemistry of Small Molecules* (Wiley, New York, 1978).
[45] M. Whitaker, M. A. Biondi, and R. Johnsen, Phys. Rev. A **24**, 743 (1981).
[46] Y. S. Cao and R. Johnsen, J. Chem. Phys. **95**, 7356 (1991).